J Biomol NMR (2017) 67:295–307
DOI 10.1007/s10858-017-0104-y

ARTICLE

Longitudinal relaxation optimized amide ^{1}H-CEST experiments for studying slow chemical exchange processes in fully protonated proteins

Tairan Yuwen[1] · Lewis E. Kay[1,2]

Received: 23 January 2017 / Accepted: 6 March 2017 / Published online: 29 March 2017

Abstract Chemical Exchange Saturation Transfer (CEST) experiments are increasingly used to study slow timescale exchange processes in biomolecules. Although ^{15}N- and ^{13}C-CEST have been the approaches of choice, the development of spin state selective ^{1}H-CEST pulse sequences that separate the effects of chemical and dipolar exchange [T. Yuwen, A. Sekhar and L. E. Kay, Angew Chem Int Ed Engl 2016 doi: 10.1002/anie.201610759 (Yuwen et al. 2017)] significantly increases the utility of ^{1}H-based experiments. Pulse schemes have been described previously for studies of highly deuterated proteins. We present here longitudinal-relaxation optimized amide ^{1}H-CEST experiments for probing chemical exchange in protonated proteins. Applications involving a pair of proteins are presented establishing that accurate ^{1}H chemical shifts of sparsely populated conformers can be obtained from simple analyses of ^{1}H-CEST profiles. A discussion of the inherent differences between ^{15}N-/^{13}C- and ^{1}H-CEST experiments is presented, leading to an optimal strategy for recording ^{1}H-CEST experiments.

Keywords ^{1}H chemical exchange saturation transfer · Slow exchange · Rare conformational states · Protein dynamics

Electronic supplementary material The online version of this article (doi:10.1007/s10858-017-0104-y) contains supplementary material, which is available to authorized users.

✉ Lewis E. Kay
kay@pound.med.utoronto.ca

[1] Departments of Molecular Genetics, Biochemistry and Chemistry, University of Toronto, Toronto, ON, Canada

[2] Hospital for Sick Children, Program in Molecular Structure and Function, Toronto, ON, Canada

Introduction

Biomolecular dynamics occur over a broad spectrum of timescales and are important in mediating a wide range of diverse functions (Henzler-Wildman and Kern 2007; Karplus and Kuriyan 2005; Kimsey et al. 2015; Sekhar and Kay 2013; Tzeng and Kalodimos 2013). Recognizing the importance of motion for function, a large number of different biophysical techniques have emerged to study processes with timescales ranging over many orders of magnitude, from rapid pico- to nano-second dynamics to hydrogen exchange that occurs on the seconds timescale (or longer). A central player in this field has been NMR spectroscopy, as it offers unparalleled capabilities for the study of motion spanning a wide range of timescales with atomic resolution and in a manner which most often does not require attachment of bulky probes that can perturb the very processes that are of interest (Anthis and Clore 2015; Mittermaier and Kay 2006; Palmer et al. 2001). Many of the recent methodological advances in solution NMR studies of molecular dynamics have focused on studies of conformational exchange where a number of different experiments such as Carr Purcell Meiboom Gill (CPMG) (Carr and Purcell 1954; Meiboom and Gill 1958) and $R_{1\rho}$ relaxation dispersion (Deverell et al. 1970; Palmer and Massi 2006), magnetization exchange (Farrow et al. 1994; Montelione and Wagner 1989), Dark State Exchange Saturation Transfer (DEST) (Fawzi et al. 2011) and Chemical Exchange Saturation Transfer (CEST) (Vallurupalli et al. 2012) have become popular, with each technique offering unique advantages that are suitable for the quantitative study of dynamics within specific time windows.

In the past several years our laboratory has focused on the development of CEST-based experiments that are most suitable for characterizing conformational exchange

processes with rates that are in the range of ~50–400 s^{-1} (Vallurupalli et al. 2012). This approach dates to the early 1960s with the pioneering studies of Forsen and Hoffman (Forsen and Hoffman 1963) and then subsequently to the important work of Gupta and Redfield in the 1970s (Gupta and Redfield 1970) where the method was extended to protein applications. The recognition by Balaban and coworkers that CEST could be used to amplify very weak signals by observing them through a much more intense reporter (Ward et al. 2000) has led to applications in the field of MRI (van Zijl and Yadav 2011). The idea of amplification is also critically important for CEST applications to biomolecular exchange where sparsely populated, transiently formed excited states are 'visualized' through spectra that derive from the populated, long lived ground state. CEST applications to proteins and nucleic acids have focused primarily on ^{15}N (Vallurupalli et al. 2012) and ^{13}C (Bouvignies and Kay 2012a; Bouvignies et al. 2014; Vallurupalli and Kay 2013; Zhao et al. 2014; Zhao and Zhang 2015) probes since their low gyromagnetic ratios ensure that they report only on chemical exchange processes with little or no contributions from magnetization exchange that arise through dipolar interactions. Although ^{1}H spins are both unique and sensitive reporters of conformation, with chemical shifts sensitive to ring current effects and, in the case of amides, to hydrogen bond formation (Wishart 2011), applications of ^{1}H CEST to the study of conformational exchange have been limited. This is due to the appearance of significant 'artifacts' from ^{1}H–^{1}H cross-relaxation of the proton spins of interest, with neighboring protons giving rise to dips in the resulting CEST profiles that often obscure those derived from chemical exchange (Bouvignies and Kay 2012b).

Recently NMR experiments have been reported that separate chemical and dipolar magnetization exchange so that ^{1}H CEST profiles can be recorded that are completely free of NOE artifacts (Yuwen et al. 2017), even in large protein systems where extensive dipolar relaxation pathways are operative. The approach, demonstrated for amide protons in ^{15}N-labeled proteins, isolates a pair of pathways involving amide ^{1}H magnetization coupled to ^{15}N in spin states α and β that give rise to exchange-based CEST profiles that are offset with respect to each other by $^{1}J_{HN}$, the one bond ^{1}H–^{15}N scalar coupling. In contrast, dips that arise from cross-relaxation are not offset. As described in detail previously (Yuwen et al. 2017) and summarized below, subtraction of the pair of CEST profiles thus removes NOE dips while retaining those from chemical exchange. Our previous work had focused on studies of perdeuterated proteins (Yuwen et al. 2017) and it is of interest to extend it to protonated molecules, especially as there are cases where protein expression is limiting so that deuteration becomes prohibitive. Herein we build upon the ideas of spin state selective ^{1}H-CEST that we outlined previously (Yuwen et al. 2017) along with longitudinal relaxation optimized (L-optimized) spectroscopy (Pervushin et al. 2002) that is used so elegantly in the BEST-family of experiments (Lescop et al. 2007) to present a pair of amide-based ^{1}H CEST pulse schemes that can be recorded on fully protonated proteins. Because ^{1}H-CEST is more efficiently recorded in ways that are slightly different than for ^{15}N- or ^{13}C-CEST these differences are highlighted below in a discussion of how to optimize sensitivity, along with applications to a number of protonated proteins.

Materials and methods

Sample preparation

An NMR sample of [U-^{15}N] human telomere repeat binding factor (hTRF1) was prepared as described previously (Sekhar et al. 2016), comprising 1.0 mM protein dissolved in 50 mM sodium acetate, 1.0 mM EDTA, 50 mM NaCl, 1 mM NaN_3, pH 5.7, 90% H_2O/10% D_2O. An NMR sample of [U-^{15}N] C6A/C57A/C111S/C146S superoxide dismutase (SOD1) that is metal free and reduced (apoSOD1^{2SH}) was prepared as described previously (Sekhar et al. 2015b), with 1.4 mM protein dissolved in 20 mM HEPES, 1 mM NaN_3, pH 7.4, 90% H_2O/10% D_2O. An NMR sample of [U-^{2}H; Ileδ1-$^{13}CHD_2$; Leu, Val-$^{13}CHD_2$/$^{12}CHD_2$; Met-$^{13}CHD_2$] G48A Fyn SH3 domain was prepared as discussed in the literature (Bouvignies et al. 2014), with 1.35 mM protein dissolved in 50 mM sodium phosphate, 0.2 mM EDTA, 0.05% NaN_3, pH 7.0, 90% H_2O/10% D_2O (note that methyl labeling is not required for this experiment).

NMR spectroscopy

A ^{1}H-CEST dataset was recorded on hTRF1 using a 600 MHz Bruker Avance III spectrometer equipped with a triple-axis gradient cryogenically cooled probe, 35 °C. The non-TROSY scheme of Fig. 2 was used with a weak B_1 field of 31.5 Hz, along with a CEST relaxation element of duration T_{Ex} = 400 ms. Experiments were obtained as interleaved pseudo-4D datasets by recording a pair of components that are then manipulated to separate $IN^{I\alpha}$ and $IN^{I\beta}$ pathways and by varying the position of the weak ^{1}H CEST field during T_{Ex} for each 2D spectrum (over the range of 5.5–10.5 ppm) in step sizes of 30 Hz. In addition a 2D reference dataset was recorded with a B_1 offset of −12 kHz that is equivalent to setting B_1 = 0 Hz. This dataset was used to rescale the CEST baseline to 1.0 for each of the $IN^{I\alpha}$ and $IN^{I\beta}$ profiles, as discussed below (Yuwen et al. 2017). Each 2D dataset was recorded with two transients/FID, a relaxation delay of 0.4 s (although a delay of 0 s is optimal,

see text below) and (640, 64) complex points in (t_2, t_1) to give a net acquisition time of ~4 min/spectrum. The net measurement time for each CEST dataset was ~14 h.

^{1}H CEST experiments were measured for C6A/C57A/C111S/C146S apoSOD1^{2SH} using an 800 MHz Bruker spectrometer equipped with a z-axis cryogenically cooled probe, 25 °C. A ^{1}H dataset was recorded with the TROSY scheme of Fig. 1, using a weak B_1 field of 30.4 Hz, T_{Ex} = 400 ms. A pseudo-4D dataset was recorded by obtaining pairs of interleaved spectra derived from either $IN^{I\alpha}$ or $IN^{I\beta}$ magnetization transfer pathways and by varying the position of the ^{1}H offset during T_{Ex} after each pair of 2D spin-state selective datasets was obtained. A range of ^{1}H offsets spanning 5.5–11.3 ppm was chosen, with step sizes of 30 Hz. An additional reference 2D dataset was obtained by setting the B_1 offset to −12 kHz. Each 2D dataset was recorded with 4 transients/FID, a relaxation delay of 0 s and (768, 64) complex points in (t_2, t_1) to give a net acquisition time of ~4 min/spectrum. The total measurement time for each pseudo-4D was ~24 h.

^{1}H CEST experiments were measured for the G48A Fyn SH3 domain using a 600 MHz Bruker spectrometer, 25 °C. ^{1}H experiments were recorded with non-L-optimized schemes, as the sample was highly deuterated, using either the non-TROSY ^{1}H CEST scheme as described previously (Yuwen et al. 2017) or a slightly modified sequence which includes an additional amide selective inversion pulse applied in alternate scans immediately prior to T_{Ex} and a modified phase cycle that effectively drives H_z magnetization to zero during T_{Ex}. A B_1 field of 26.2 Hz along with T_{Ex} = 400 ms were chosen. Experiments were obtained as interleaved pseudo-4D datasets as above with the position of the weak ^{1}H CEST field varied over a range of 5.7–10.5 ppm, step size of 25 Hz, along with an additional 2D reference dataset recorded with a B_1 offset of −12 kHz. Each 2D dataset was recorded with two transients/FID, a relaxation delay of 1.0 s and (640, 32) complex points in (t_2, t_1) to give a net acquisition time of ~3 min/spectrum. The net measurement time for each CEST dataset was ~13 h.

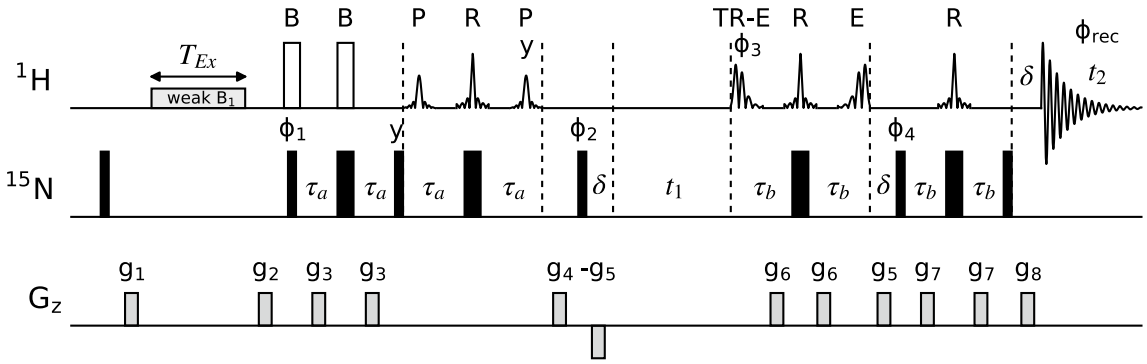

Fig. 1 TROSY L-optimized spin state selective ^{1}H-CEST experiment for studies of slow chemical exchange in protonated proteins. 90° (180°) rectangular pulses on the ^{15}N channel (119 ppm), denoted by *narrow* (*wide*) *black rectangles*, are applied at maximum power. The pulses on the ^{1}H channel are, in order of execution, BIP (Smith et al. 2001), PC9 (Kupce and Freeman 1993), REBURP, time reversed (TR) EBURP (Geen and Freeman 1991), and EBURP, denoted as B, P, R, TR-E and E, and implemented as in BEST-TROSY (Favier and Brutscher 2011); actual shapes are displayed in the pulse diagram. The ^{1}H carrier is positioned on the water resonance, with the exception of the CEST element where it is moved to the desired frequency. PC9, REBURP and EBURP pulses are generated with phase modulation for off-resonance excitation that covers only the $^1H^N$ region (centered at ~8.4 ppm). The typical durations of the shaped pulses (600 MHz) are: BIP: 200 µs; PC9: 3.0 ms; REBURP: 2.0 ms; EBURP: 1.92 ms, that results in excitation of ~4 ppm (Schanda et al. 2006). Durations of τ_a and τ_b are adjusted to account for the active J-coupled evolution during the shaped pulses, corresponding to 0.5, 1.0 and 0.67 of the PC9, REBURP and EBURP pulse widths, respectively (Lescop et al. 2010). The delays used are: $\tau_a \simeq \tau_b \simeq 1/(4^1J_{HN})$=2.70 ms. All pulses are applied with phase x unless otherwise indicated. The following phase cycle is used: φ_2 = y, −y, −x, x; φ_3 = y; φ_4 = y; φ_{rec} = y, −y, x, −x. Quadrature detection in F_1 is achieved by inverting the phases of φ_3, φ_4, φ_{rec} along with gradient g_8 (Kay et al. 1992; Schleucher et al. 1993) and changing φ_2 to y, −y, x, −x. A minimum 4 step cycle is recommended for optimal TROSY selection, however two steps is sufficient as coherence selection gradients (g_5, g_8) are applied. Two CEST profiles, corresponding to selection of $IN^{I\alpha}$ and $IN^{I\beta}$ pathways are collected by setting φ_1 to −x or x, respectively, and storing the resulting datasets in separate memory locations. Gradients are applied with the following durations (ms) and strengths (% maximum): g_1: (0.4, −25%), g_2: (1.0, 15%), g_3: (1.0, −60%), g_4: (1.5, −70%), g_5: (0.256, 40%), g_6: (0.256, 60%), g_7: (0.256, 15%), g_8: (0.256, 31.9%) with the strength of g_8 changed to 48.1% for collecting the quadrature component in t_1. The gradient strengths g_6 and g_7 are chosen according to Mulder et al. (Mulder et al. 2011) in order to minimize weak F_2 phasing artifacts. The weak ^{1}H B_1 field was calibrated using the approach of Guenneugues et al. (Guenneugues et al. 1999). Note that a small zero order phase correction in the F_1 dimension is required to obtain pure absorptive line-shapes due to $^1J_{HN}$ evolution of the TROSY component of ^{15}N transverse magnetization during the first δ element, corresponding to $\delta \times {}^1J_{HN} \times 180°$ (−8.4° for δ = 500 µs)

Data analysis

All NMR spectra were processed and analyzed using the NMRPipe suite of programs (Delaglio et al. 1995). Analysis of CEST profiles was carried out using the software package *ChemEx* (https://github.com/gbouvignies/chemex); a separate module is required for fitting the difference ^{1}H-CEST profiles, $IN^{I\beta} - IN^{I\alpha}$, which is available upon request. As described above, a reference plane is recorded with the full CEST duration but without the weak B_1 field, typically obtained by placing the B_1 field far off-resonance (*e.g.* −12 kHz), from which cross-peak intensities are quantified, $I(T_{Ex},B_1=0)$. The ratio of major state cross-peak intensities, $I(T_{Ex},B_1)/I(T_{Ex},B_1=0)$, is plotted as a function of the position of the weak B_1 field, to generate CEST profiles that are scaled identically for both $IN^{I\beta}$ and $IN^{I\alpha}$ pathways (Yuwen et al. 2017). A difference ^{1}H-CEST profile is calculated and subsequently fit, as described in detail previously (Yuwen et al. 2017), to extract chemical shifts of the excited state. CEST profiles can be fit using ^{1}H R_1 rates as fitting parameters or by fixing rates to values measured using separate pulse schemes, with very similar chemical shifts obtained in both cases.

Results and discussion

L-optimized ^{1}H-CEST for studies of fully protonated proteins

In a previous publication we presented amide ^{1}H-CEST experiments for studies of conformational exchange in ^{15}N labeled proteins (Yuwen et al. 2017). Applications focused on highly deuterated molecules since deuteration is particularly important in studies of high molecular weight systems that are of interest to our laboratory. Additionally, as discussed previously, high levels of deuteration minimize ^{1}H–^{1}H cross-relaxation during the ^{1}H-CEST relaxation element, an effect that decreases the sizes of dips from the minor state that provide much of the important information in CEST (Yuwen et al. 2017). However, recognizing that production of deuterated biomolecules is not an option in some cases, we sought to extend previously described ^{1}H-CEST sequences to include L-optimized pulse schemes (Pervushin et al. 2002) for measurements on fully protonated proteins, including both TROSY (Fig. 1) and non-TROSY (Fig. 2) versions. The experiments are similar to our previous sequences (Yuwen et al. 2017) with ^{1}H pulses replaced by the appropriate amide selective shaped pulses, as implemented in BEST-TROSY (Favier and Brutscher 2011) and BEST-HSQC (Schanda et al. 2006) pulse schemes.

Figures 1 and 2 present the L-optimized ^{1}H-CEST pulse sequences that have been developed for studies on fully protonated proteins. The TROSY-based scheme, Fig. 1, is executed as a pair of experiments that separates magnetization flow on the basis of the spin state of the nitrogen heteroatom attached to the amide proton spin of interest. In the first experiment amide proton magnetization from proton spin I coupled to its attached ^{15}N in the up state (referred to as $N^{I\alpha}$ in what follows) is transferred immediately after the CEST element of duration T_{Ex} to the ^{15}N TROSY component via an ST2 scheme (Pervushin et al. 1998) and then subsequently to the ^{1}H TROSY line (Pervushin et al. 1997) for detection. In a second experiment magnetization from spin I coupled to $N^{I\beta}$ is selected and transferred in the same manner via a spin-state selective pathway that uses the TROSY component exclusively as well. The two pathways can therefore be summarized succinctly by the following flow diagram

$$^1H\ CEST \rightarrow I_zN^{Ii} \xrightarrow{ST2} N_x^I I^\beta \rightarrow I_xN^{I\beta}, i \in \{\alpha,\beta\} \quad (1)$$

and they give rise to a pair of CEST profiles that will be referred to in what follows as $IN^{I\alpha}$ and $IN^{I\beta}$, offset with respect to each other by $^1J_{HN}$ (see below). A similar scheme has been implemented for applications involving small proteins, where a non-TROSY, sensitivity enhanced sequence has been developed, Fig. 2. Here both IN^{Ii}, $i \in \{\alpha,\beta\}$ pathways are retained throughout the pulse scheme and then separated at the end using either IP/AP (Ottiger et al. 1998; Yang and Nagayama 1996) or S^{3}E (Felli and Pierattelli 2015) based approaches. In this manner the non-TROSY experiment is as much as $\sqrt{2}$ more sensitive than a sequence that records the pathways separately. Note that the isolation of the two pathways described above is predicated on the absence of ^{15}N spin-flips (*i.e.*, small ^{15}N R_1 rates). In practice, finite rates will lead to sensitivity decreases without compromising the accuracy of extracted ^{1}H chemical shifts of excited states that is the primary motivation for these experiments. Further details are provided in Yuwen et al. (Yuwen et al. 2017).

As described above, the longitudinal relaxation enhancement approach used in these experiments was initially implemented in L-TROSY pulse schemes (Pervushin et al. 2002) and subsequently extended to the BEST-family of experiments (Lescop et al. 2007) where their high performance arises from the application of selective pulses covering only the ^{1}H^N region in fully protonated proteins. In this manner both water and carbon-bound protons are preserved at near equilibrium values that then serve to enhance the recovery of amide protons. Thus, a very short recycling delay can be used to achieve optimal sensitivity per unit measurement time (Schanda et al. 2006), that is compatible with ^{1}H CEST experiments, since decoupling is not

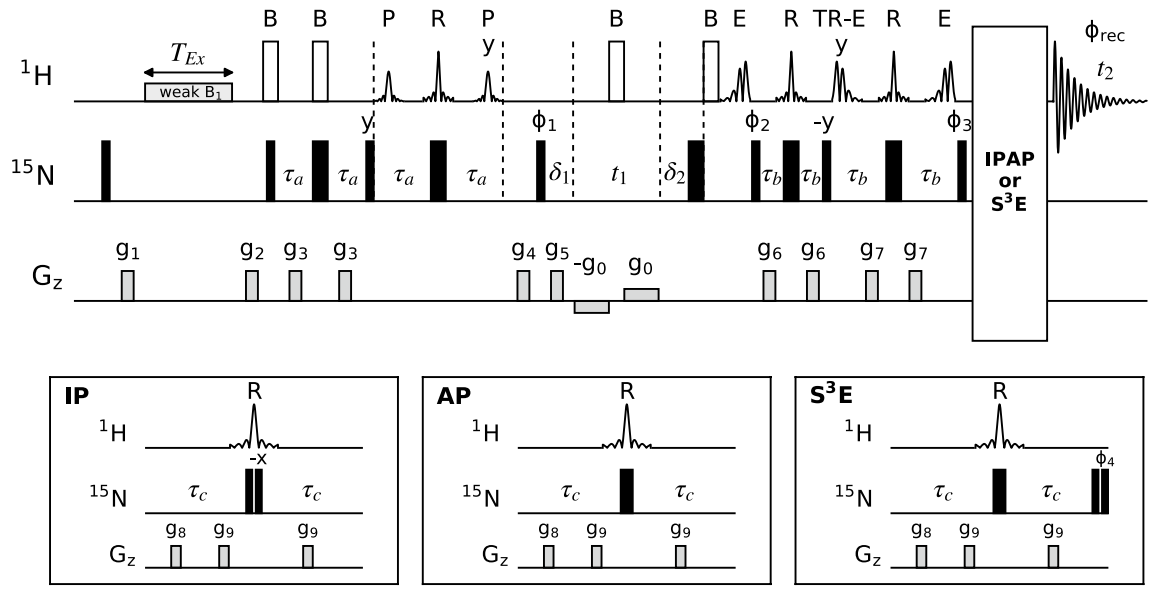

Fig. 2 Non-TROSY, L-optimized spin state selective ^{1}H-CEST experiment. Many of the details of the pulse scheme are similar to those described for the scheme of Fig. 1 and will not be repeated. Prior to t_1 evolution the pulse scheme is essentially identical to the sequence of Fig. 1 with both $IN^{I\alpha}$ and $IN^{I\beta}$ spin state components of magnetization transferred via ST2 polarization transfer (Pervushin et al. 1998) to ^{15}N for chemical shift evolution (t_1). After the t_1 period both pathways are retained for the duration of the pulse scheme, as described previously (Yang and Kay 1999), and these are subsequently separated via IPAP (Ottiger et al. 1998; Yang and Nagayama 1996) or S^{3}E (Felli and Pierattelli 2015) elements at the end of the sequence. Preserving both pathways on a per-scan basis improves the signal to noise by as much as $\sqrt{2}$ relative to the case where each pathway is measured independently. Values of the delays are $\tau_a \simeq \tau_b \simeq 1/(4^1J_{HN}) = 2.70$ ms. All pulses are applied with phase x unless otherwise indicated. The following phase cycle is used: φ_1 = x, −x; φ_2 = −x. Quadrature detection in F_1 is achieved by inverting the phase of φ_2 together with the sign of gradient g_8 (Kay et al. 1992; Schleucher et al. 1993); g_9 is inverted in concert with g_8. Separation of $IN^{I\alpha}$ and $IN^{I\beta}$ pathways can be achieved using either IPAP (Ottiger et al. 1998; Yang and Nagayama 1996) ($\tau_c = 1/(4^1J_{HN}) = 2.70$ ms) or S^{3}E (Felli and Pierattelli 2015) ($\tau_c = 1/(8^1J_{HN})$) schemes, each with similar performance in terms of pathway selection. Note that a value of $\tau_c = 1.39$ ms was found to be optimal for the S^{3}E scheme in terms of isolating each of the two pathways. The delay times δ_1 and δ_2 are set as (1+λ)/2 and (1−λ)/2 of the duration of the EBURP pulse, respectively, where λ = 0.67 is the fraction of active J-coupled evolution time during the EBURP (Lescop et al. 2010). In the IPAP version $\varphi_3 = -x$; φ_{rec} = x, −x for recording in-phase (IP) spectra, while φ_3 = x; φ_{rec} = y, −y for recording anti-phase (AP) spectra. In the S^{3}E version a pair of datasets are recorded with $\varphi_3 = -x$; φ_4 = x; φ_{rec} = x, −x and with φ_3 = x; $\varphi_4 = -x$; φ_{rec} = y, −y. For IPAP and S^{3}E approaches the separately recorded datasets are added and subtracted to give CEST spectra corresponding to $IN^{I\alpha}$ and $IN^{I\beta}$ pathways. Gradients g_1–g_4 are the same as for the TROSY scheme of Fig. 1, while the durations (ms) and strengths (in % maximum strength) of the remaining gradients are g_5: (1.25, 80%), g_6: (0.256, 60%), g_7: (0.256, 15%), g_8: (0.256, −39.5%), g_9: (0.4, 30%), g_0=0.25%

applied at any stage of the experiment and thus sample heating effects are not a concern. In fact, as will be discussed below, an optimal strategy is one where the relaxation delay is set to 0, with T_{Ex} selected primarily according to the operative amide ^{1}H longitudinal relaxation rates in the system studied to achieve maximum sensitivity in ^{1}H CEST profiles.

Experimental applications

In order to demonstrate the performance of the L-optimized ^{1}H CEST experiments in studies of fully protonated proteins we first recorded spectra on the human telomere repeat binding factor (hTRF1), a small four helix protein that folds on the ms timescale (Sekhar et al. 2016) according to a classical two-state model, $G \underset{k_{EG}}{\overset{k_{GE}}{\rightleftarrows}} E$, where states G ('ground') and E ('excited') correspond to the natively folded conformer and an ensemble of unfolded conformations, respectively. Exchange parameters, (p_E, $k_{ex} = k_{GE} + k_{EG}$) = (4.2%, 346 s^{-1}), where p_E is the population of the excited (unfolded) state, have been obtained from a joint analysis of ^{15}N- and ^{13}C-CEST datasets (Sekhar et al. 2015a). In the analysis of profiles from the ^{1}H-CEST dataset recorded using the scheme of Fig. 2 minor state dips were observed for 37 residues. Figure 3a, b highlights profiles from a pair of these residues showing the displacements between $IN^{I\alpha}$ (*blue*) and $IN^{I\beta}$ (*red*) curves (*top*) along with the difference between the profiles ($IN^{I\beta}$–$IN^{I\alpha}$) that subtracts out any NOE dips. Note that, as described previously (Yuwen et al. 2017) and briefly above, $IN^{I\alpha}$ and $IN^{I\beta}$ profiles are offset by $^1J_{HN}$ so that both major and minor dips in the difference profile have anti-phase absorptive shapes. The nature of this doublet lineshape does place a

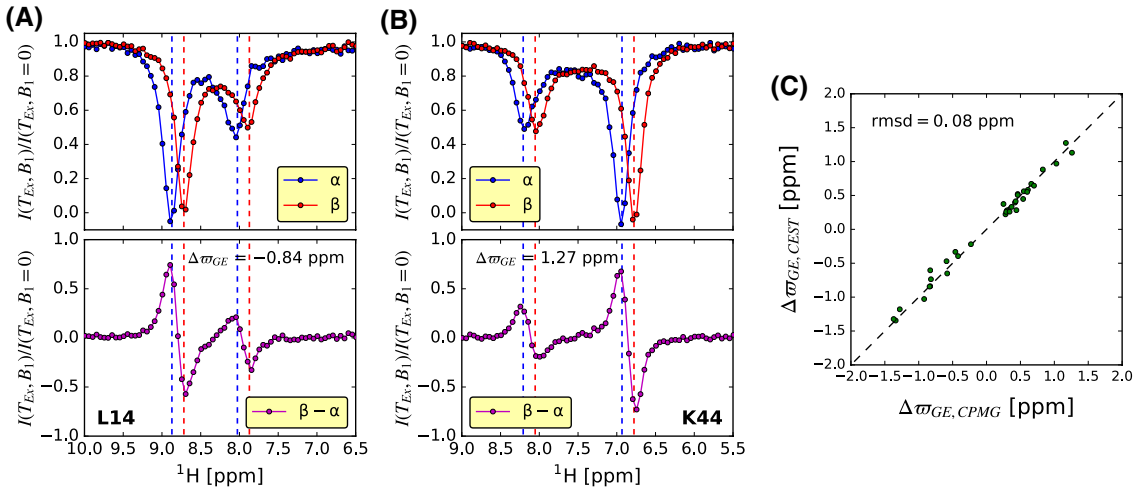

Fig. 3 **a**–**b** Representative spin state selective ^{1}H CEST profiles (*top*) and difference profiles (*bottom*) measured on a sample of fully protonated hTRF1 using the scheme of Fig. 2, 35 °C, 600 MHz, T_{Ex} = 400 ms, weak B_1 field = 31.5 Hz. The positions of ground and excited states are indicated with *dashed lines in blue or red* for ^{15}N spin state α or β respectively. Values of $\Delta\varpi_{GE}$ obtained from fits are indicated in *each panel*. **c** Linear correlation plot of $\Delta\varpi_{GE}$ values obtained via $^{1}H^{N}$ CEST and $^{1}H^{N}$ CPMG experiments

limit of approximately 0.2 ppm on the minimum $\Delta\varpi_{GE}$ ($= \varpi_E - \varpi_G$) for which minor state CEST dips can be quantified; nevertheless a significant number of excited state chemical shifts could be obtained for hTRF1 and for a 150 residue protein (53 values), described below. Because hTRF1 is a small protein (53 residues) and a relatively high temperature is used there are few strong NOE dips in this case and the positions of the exchange dips are thus clear from individual profiles (but see below). Figure 3c shows a linear correlation plot of ^{1}H $\Delta\varpi_{GE}$ values obtained from analysis of CEST and CPMG profiles and excellent agreement (rmsd = 0.08 ppm) is noted.

Having demonstrated that the L-optimized ^{1}H CEST experiment generates high quality ^{1}H CEST profiles for a fully protonated small protein, we next recorded ^{1}H CEST spectra of the most immature form of the antioxidant metalloenzyme superoxide dismutase (SOD1), lacking metal and a stabilizing intra-subunit disulfide bond (apoSOD1^{2SH}). We have shown previously that this form of the enzyme is highly dynamic with the ground state interconverting with a series of sparsely populated and transiently formed conformers (Sekhar et al. 2015b). Because apoSOD1^{2SH} does not express particularly well production of perdeuterated protein becomes expensive, providing impetus for the development of the L-optimized schemes discussed in the text. For this system (153 residues) the TROSY-experiment was more sensitive than the non-TROSY version so that the sequence of Fig. 1 was used to record ^{1}H-CEST profiles, 25 °C. Figure 4a–e shows representative $IN^{I\alpha}$ (*blue*) and $IN^{I\beta}$ (*red*) profiles (*top*) along with the difference between the profiles ($IN^{I\beta}$–$IN^{I\alpha}$) (*bottom*) that removes the NOE dips. Analysis of difference profiles is particularly important in the case of R115 where it is difficult to separate exchange and dipolar relaxation mediated dips from either of the IN^{Ii}, $i \in \{\alpha, \beta\}$, profiles individually. In total CEST dips could be quantified for 53 residues and the ^{1}H $\Delta\varpi_{GE}$ values so obtained are in good agreement with predicted values assuming that the sparse state corresponds in structure to the mature form of the enzyme, whose chemical shifts have been obtained by Banci and coworkers (Banci et al. 2002), Fig. 4f. It is worth noting that we do not recommend fitting (p_E, k_{ex}) values from ^{1}H-CEST profiles, as ^{1}H cross-relaxation leads to a decrease in the sizes of the minor state dips (Yuwen et al. 2017). Such effects are difficult to take into account properly as relaxation of ^{1}H longitudinal magnetization is, in general, non-exponential. We prefer, therefore, to measure exchange parameters from ^{15}N-CEST experiments.

Comparison between ^{1}H- and ^{15}N-/^{13}C-based CEST experiments

The basic CEST experiment records the response of longitudinal magnetization to radio frequency irradiation during a delay period in which magnetization decays back to its equilibrium value, M_o. However, by recording spectra using a phase cycle in which the longitudinal magnetization of interest is inverted in successive scans prior to the CEST element the signal, averaged over the pair of scans, effectively decays to zero during T_{Ex} rather than to M_o (Freeman and Hill 1971; Sklenar et al. 1987; Vallurupalli et al. 2012). This leads to a simplification in fits of the resulting CEST profiles since they no longer depend on the equilibrium magnetization, eliminating one fitting parameter and leading to more

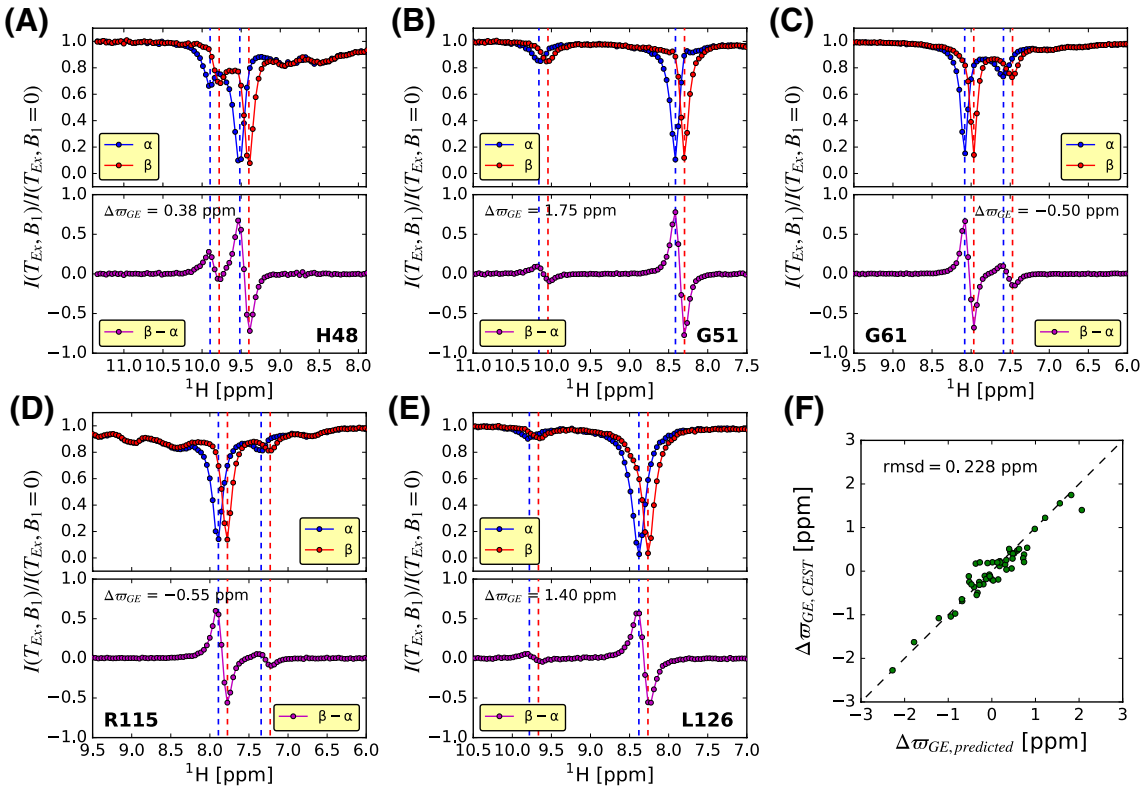

Fig. 4 **a–e** Representative spin state selective ^{1}H CEST profiles (*top*) and difference profiles (*bottom*) measured on a sample of fully protonated apoSOD1^{2SH} using the scheme of Fig. 1, 25 °C, 800 MHz, T_{Ex} = 400 ms, weak B_1 field = 30.4 Hz. **f** Linear correlation of $\Delta\varpi_{GE}$ values measured from ^{1}H-CEST with predicted values assuming that the sparse state corresponds in structure to the mature form of the enzyme, whose chemical shifts have been obtained by Banci et al. (2002)

accurate quantitation of (p_E, k_{ex}) values. All of the *X*-(^{15}N-, ^{13}C-) based CEST experiments developed to date exploit this two-step cycle and the simplification in data fitting that results (Bouvignies et al. 2014; Vallurupalli et al. 2012). In applications involving ^{1}H spins, however, such an approach is not optimal as described below. In what follows we assume a two state exchange reaction with z magnetization from states *G* and *E* in the ratio $M_z^G/M_z^E \approx p_G/(1-p_G)$ at the start of the T_{Ex} period, where M_z^k is the longitudinal ^{15}N, ^{13}C or ^{1}H magnetization and $k \in \{G, E\}$. We calculate the intensities of minor state CEST dips for *X*- and ^{1}H-CEST experiments when longitudinal magnetization recovers to its (i) equilibrium value or (ii) decays to zero (2 step phase cycle) during T_{Ex} (see SI for details), highlighting key differences between *X*- and ^{1}H-CEST. The calculation is straightforward for ^{15}N and ^{13}C CEST because the low gyromagnetic ratio of spin *X* ensures that cross-relaxation with neighboring like spins is, in general, minimal so that a consideration of the evolution of an isolated spin is sufficient (Vallurupalli et al. 2012). In contrast, an extensive network of ^{1}H–^{1}H dipolar interactions complicates a rigorous simulation of ^{1}H-CEST, in particular for the case of a fully protonated protein. As described in SI a simple model has been chosen where it is assumed that the amide proton, *I*, of interest is dipolar coupled to a large number, *N*, of non-amide proton spins, *S*. Thus, for scheme (ii) and, in the case of amide ^{1}H-CEST, only the amide proton is inverted in successive scans while all non-amide protons remain at equilibrium and effectively serve to decrease the effective longitudinal relaxation time of spin *I*. While undoubtedly a simplification, this model is appealing in that it is simple to analyze mathematically and it does illustrate the important differences between *X*- and ^{1}H-CEST experiments.

Following the assumptions given above, and elaborated on in detail in SI, intensities of minor state CEST dips, I^{CEST}, are given for both *X* and ^{1}H-CEST by

$$I^{CEST}(T_{Ex})/M_o = \left[\frac{k_{GE}}{\rho_j + k_{GE}} + e^{-\rho_j T_{Ex}}(\kappa - 1) - e^{-(\rho_j + k_{GE})T_{Ex}} \left(\kappa - \frac{\rho_j}{\rho_j + k_{GE}}\right)\right] \tag{2}$$

and

$$I^{CEST}(T_{Ex})/M_o = \kappa e^{-\rho_j T_{Ex}}(1 - e^{-k_{GE}T_{Ex}}) \tag{3}$$

for schemes (i) and (ii), respectively, where M_o is the equilibrium magnetization. In Eqs. 2 and 3 κ is defined such that

κM_o is the longitudinal magnetization immediately prior to the CEST element ($T_{Ex} = 0$). The κ factor thus accounts for the recovery of ^{1}H magnetization during the recycle delay between scans (duration d_1) and, in the case of X-CEST, the subsequent X-spin sensitivity gain from $^1\text{H} \rightarrow X$ polarization transfer that precedes the CEST delay, with $\kappa = \{1 - \exp(-\rho_H d_1)\}|\gamma_H/\gamma_j|$, $j \in \{^{15}N, ^{13}C, ^1H\}$. Thus, κ is larger for ^{15}N or ^{13}C than for ^{1}H because X magnetization at the start of the CEST element is much further from its equilibrium value than for ^{1}H-CEST. In Eqs. 2 and 3 ρ_j is the auto-relaxation of M_z. As discussed above and in detail in SI we distinguish between two 'classes' of protons, corresponding to amide, I, and non-amide, S, spins and in what follows ρ_H is the relaxation rate of the amide spin I of interest. When necessary the relaxation rates of spins I and S, are explicitly denoted by ρ_I and ρ_S, respectively. In general, $\rho_H \gg \rho_X$ with large contributions to ρ_H from cross-relaxation with neighboring protons that are absent for ρ_X. Thus when amide proton spin I is inverted and non-amide protons are not, spin I will relax rapidly to equilibrium, significantly decreasing the intensity of the minor state CEST dip. Large differences are predicted, therefore, between schemes (i) and (ii) in the ^{1}H case with significantly increased sensitivity for scheme (i). Interestingly, for a given spin type j the sensitivity difference between the schemes, $\Delta I^{CEST} = I^{CEST}$ (scheme i) $- I^{CEST}$(scheme ii), is independent of κ,

$$\frac{\Delta I^{CEST}(T_{Ex})}{M_o} = \frac{k_{GE}}{\rho_j + k_{GE}} - e^{-\rho_j T_{Ex}} + \frac{\rho_j}{\rho_j + k_{GE}} e^{-(\rho_j + k_{GE})T_{Ex}} \tag{4}$$

but depends critically on ρ_j. The relative sensitivity gain, $\frac{\Delta I^{CEST}}{I^{CEST}(\text{scheme ii})}$, however, scales inversely with κ so that CEST applications involving low gyromagnetic ratio spins will show only very modest relative sensitivity gains, but much larger gains would be predicted for ^{1}H experiments.

That this is the case is illustrated in Fig. 5a–c where plots of $I^{CEST}(T_{Ex})$ for ^{15}N–(a), ^{13}C–(b), and ^{1}H–(c) CEST are displayed. As can be seen for X-CEST there is a slight increase in the relative minor dip intensity when magnetization returns to its steady state value, case (i), as expected, while a much more significant relative increase is noted for ^{1}H-CEST. It is thus preferable to record ^{1}H-CEST experiments with scheme (i), as is done in the pulse sequences of Figs. 1 and 2, above, and in a previously published set of experiments (Yuwen et al. 2017). The importance of choosing an optimal scheme to record ^{1}H-CEST experiments is made clear by a comparison of CEST profiles measured on a sample of the G48A Fyn SH3 domain that exchanges between a natively folded conformer and an unfolded ensemble. Exchange parameters, $(p_E, k_{ex}) = (8.4 \pm 0.1\%, 104.5 \pm 1.6\ \text{s}^{-1})$, 25 °C have been obtained from fits of ^{15}N-CEST datasets. Because the sample is highly deuterated we have not used the L-optimized experiments developed here but rather compared results from previously published experiments (Yuwen et al. 2017) where all ^{1}H pulses are non-selective, but which preserve water, and where the amide ^{1}H magnetization recovers to its equilibrium value during the CEST element, scheme (i) (essentially Fig. 2 but with ^{1}H rectangular pulses) and where amide protons are selectively inverted in alternate scans prior to the CEST element, scheme (ii). Note that exchange with water expedites the recovery of amide ^{1}H magnetization since $\rho_H = \rho_{H,dip} + \rho_{H,\text{H-Ex}}$ in Eqs. 2 and 3, where the first and second terms on the right correspond to contributions to longitudinal relaxation from dipolar and hydrogen exchange, respectively. It is clear from Eqs. 2 and 3 that as ρ_H increases I^{CEST} decreases and that sensitivity losses will be larger using scheme (ii). That this is the case is illustrated in Fig. 6 for a number of ^{1}H-CEST profiles from amide protons of the Fyn SH3 domain with differing rates of exchange with solvent.

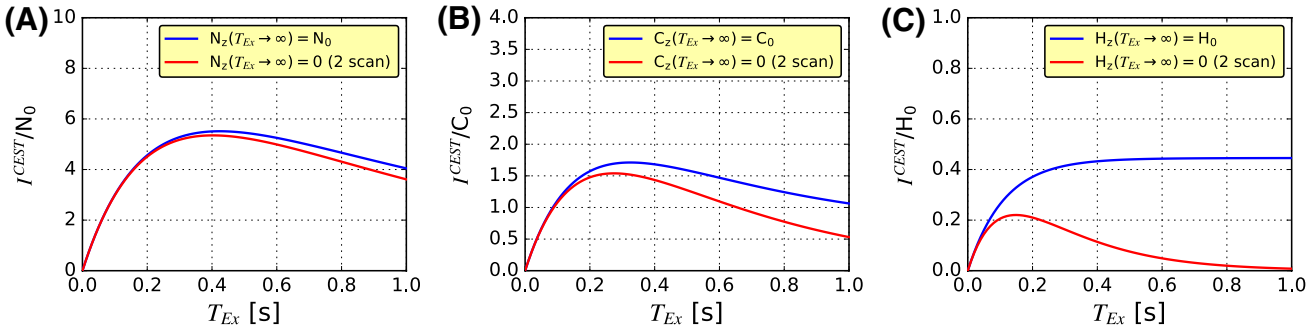

Fig. 5 Comparison of schemes (i, Eq. 2) and (ii, Eq. 3), as discussed in the text, where longitudinal magnetization returns to its equilibrium value (*blue*) or decays to zero (*red*) during T_{Ex}, respectively. Plotted are the intensities of minor CEST dips, I^{CEST}, normalized to equilibrium magnetization for ^{15}N–(**a**), ^{13}C–(**b**) and ^{1}H–(**c**) CEST. In **a**–**c** $d_1 = \infty$ has been assumed (*i.e.*, initial magnetization at the start of each scan is the equilibrium value) so that $\kappa = 10$ (**a**), 4 (**b**) and 1 (**c**). Values of ρ_j rates used in the simulations are 1, 2 and 5 s^{-1} for ^{15}N, ^{13}C and ^{1}H respectively, along with exchange parameters $p_E = 2\%$, $k_{ex} = 200\ \text{s}^{-1}$

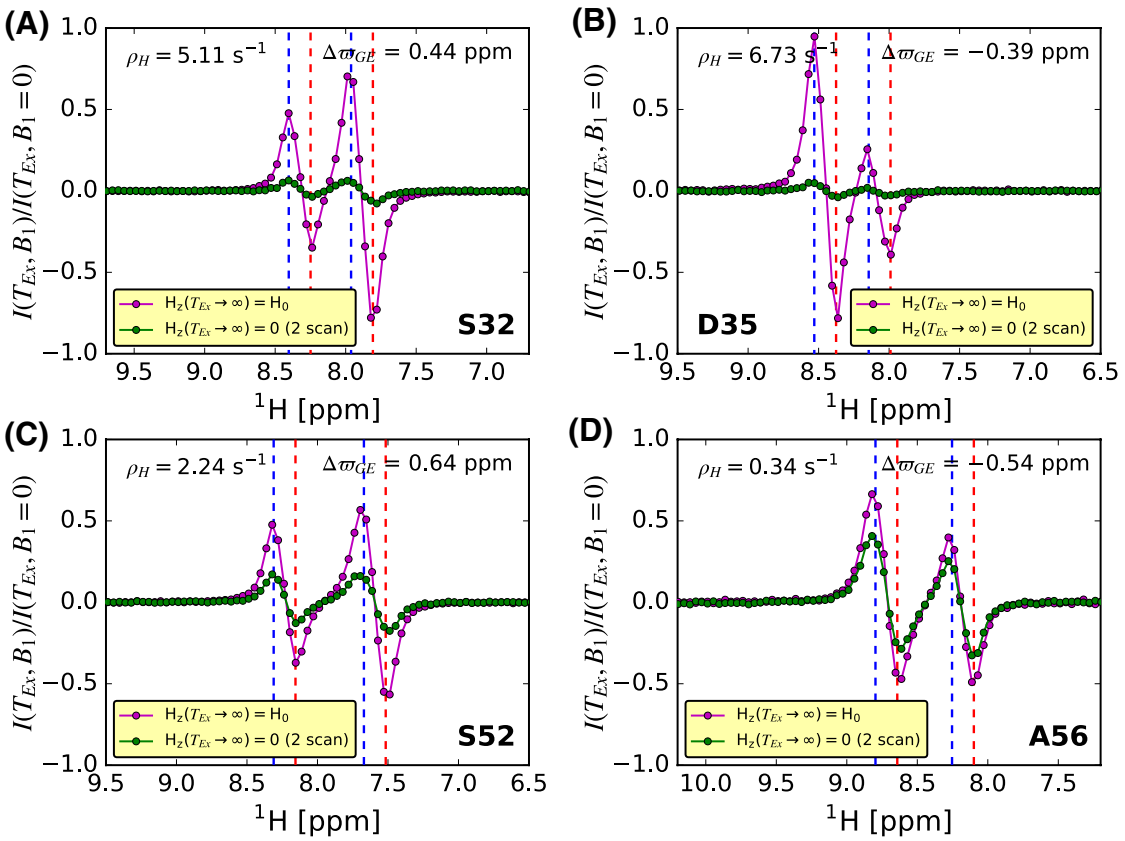

Fig. 6 Comparison of ^{1}H CEST difference profiles recorded on a sample of the G48A FynSH3 domain, 25 °C, 600 MHz, T_{Ex} = 400 ms, weak B_1 field = 26.2 Hz. The non-L-optimized pulse scheme of Yuwen et al. (Yuwen et al. 2017) (non-TROSY version) was used with magnetization evolving during the CEST element as per scheme (i), *magenta*, or scheme (ii), *green*. In the latter scheme amide protons are selectively inverted in alternate scans prior to the CEST element along with the phase of the receiver, so that longitudinal magnetization effectively relaxes to 0 during T_{Ex}. Residues selected have different ρ_H rates, mainly reflecting different solvent exchange rates. There is a strong correlation between ρ_H and the extent of attenuation of profiles recorded with scheme (ii). The two sets of ^{1}H CEST profiles for each residue have been rescaled such that the noise levels are the same. The positions of ground and excited states are indicated with *dashed lines in blue or red* for ^{15}N spin state α or β respectively

An optimal approach for recording ^{1}H CEST in studies of protonated proteins

Having established the importance of recording amide ^{1}H-CEST using pulse schemes where the magnetization recovers to its equilibrium value during the CEST relaxation element [*i.e.*, scheme (i)] we next sought to determine optimal experimental parameters in this case. A major disadvantage with recording ^{1}H-CEST on fully protonated samples is that minor state dips are attenuated from cross-relaxation of the amide proton of interest, I, with neighboring proton spins (Yuwen et al. 2017), an effect that is clearly more pronounced with increasing numbers of protons. However, it is possible to take advantage of the large network of aliphatic/aromatic ^{1}H-spins using L-optimized spectroscopy (Pervushin et al. 2002) that exploits cross-relaxation and hence the increased longitudinal relaxation rates of the amide spins of interest. Because ^{1}H magnetization returns to equilibrium during T_{Ex}, the CEST dip size I^{CEST} grows with T_{Ex} and reaches an upper bound as $T_{Ex} \to \infty$, Eq. 2, neglecting ^{15}N R_1 relaxation. For a fixed total experiment time (*i.e.* $d_1 + T_{Ex}$ is a constant), it is straightforward to show that the largest CEST dip size is always achieved for $d_1 = 0$, Fig. 7a, that is also the case in ^{1}H-CEST schemes recorded without L-optimization, Fig. 7b (*i.e.*, where there is no ^{1}H magnetization at the start of the inter-scan delay).

The optimal setup is one which maximizes the size of minor state CEST dips for a given measurement time. The appropriate value of T_{Ex} that achieves this result can be calculated for the simple case where $\Delta\varpi_{GE} \to \infty$ and for $\omega_1 \gg k_{ex}$ using Eq. 2. Although the maximum of I^{CEST} becomes smaller as ρ_H increases, I^{CEST} does reach an upper bound faster for larger ρ_H (that is effectively proportional to $-\sigma$, where σ is the rate of cross-relaxation with adjacent protons), Fig. 8a, suggesting that T_{Ex}

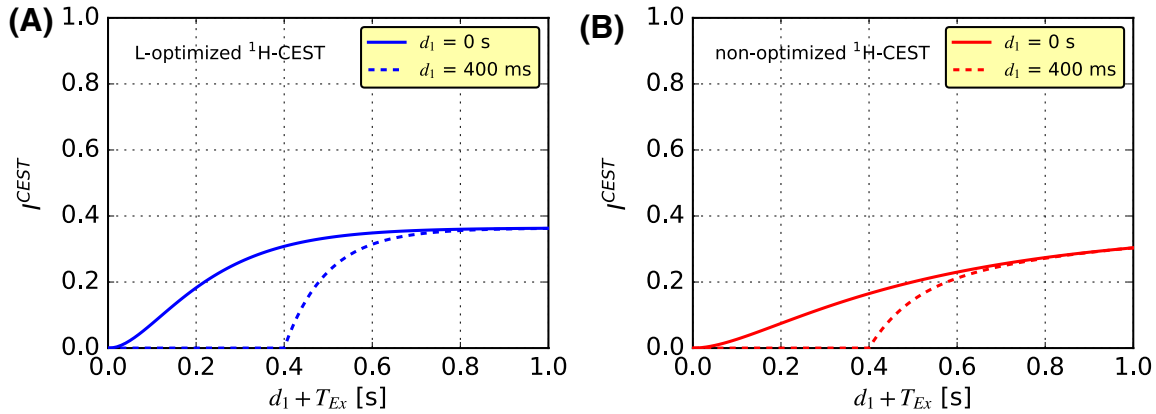

Fig. 7 Simulated I^{CEST} values assuming (**a**) L-optimized (Figs. 1, 2) and (**b**) non-L-optimized (Yuwen et al. 2017) ^{1}H CEST pulse schemes for $d_1 = 0$ s and 400 ms, showing that irrespective of the pulse scheme increased sensitivity is obtained for $d_1 = 0$ s. Values of $p_E = 2\%$, $k_{ex} = 200$ s^{-1}, $\sigma = -5$ s^{-1}, $\rho_S = \rho_I + \sigma = 2$ s^{-1} (see SI) have been used; longitudinal relaxation during the acquisition time t_2 has been neglected. The *blue curves* were generated with Eq. 2, and $\kappa = 0$ (*solid line*) or $\kappa = 1 - \exp(-\rho_H d_1)$, ρ_H (ρ_I) = 7 s^{-1}, $d_1 = 400$ ms (*dashed line*) while the *red solid curve* was obtained using Eq S17

should be adjusted with ρ_H to achieve the highest sensitivity. Figure 8b shows similar I^{CEST} curves as those in Fig. 8a (L-optimized) but for the case where all longitudinal protein ^{1}H magnetization has been destroyed at the start of acquisition (non L-optimized scheme) and it is clear that the build up of I^{CEST} with T_{Ex} is slower. For the L-optimized ^{1}H CEST experiment the optimal T_{Ex} is given by the solution to the following equation:

$$e^{-\rho_H T_{Ex}}(2\rho_H T_{Ex} + 1) - e^{-(\rho_H + k_{GE})T_{Ex}}\left(2\rho_H T_{Ex} + \frac{\rho_H}{\rho_H + k_{GE}}\right) = \frac{k_{GE}}{\rho_H + k_{GE}} \quad (5)$$

which has been derived from $\frac{d(I^{CEST}/\sqrt{T_{Ex}})}{dT_{Ex}} = 0$, and which assumes that the total time per scan is T_{Ex} (*i.e.*, $\kappa = 0$ that corresponds to $d_1 = 0$) and that the noise grows as $(T_{Ex})^{-0.5}$. Recovery of longitudinal magnetization during the (t_2) acquisition time has been neglected in the derivation. Figure 8c plots optimized T_{Ex} values as a function of $\rho_H \sim -\sigma$ for L-optimized ^{1}H-CEST and the non-optimized version (Yuwen et al. 2017). Values of T_{Ex} that give rise to optimal I^{CEST} values, I^{CEST}_{opt} corresponding to a maximum of $I^{CEST}/\sqrt{T_{Ex}}$, decrease with increasing ρ_H rates (*blue*) while the dependence is much less significant in the non-optimized experiment (*red*). I^{CEST}_{opt} values are plotted as a function of ρ_H in Fig. 8d, showing a decrease with increasing ρ_H, and importantly that the use of L-optimization results in significantly improved sensitivity per unit measurement time (for the case of protonated proteins, of course). In the discussion and derivations above we have assumed scheme (i) for recording ^{1}H-CEST that offers improved sensitivity, and we have neglected evolution of magnetization during the acquisition period, t_2, during which time longitudinal relaxation is operative. In addition, the finite t_2 period and additional delays due to t_1 chemical shift labeling and coherence transfers that extend the total pulse sequence time, and thus decrease sensitivity per unit measurement time, have also not been included. In general, because these delays are significantly smaller than T_{Ex} their omission affects the (semi-) quantitative analyses given here only slightly. By means of illustration I^{CEST}_{opt} values are plotted in Fig. 8d that take into account these additional delays (*dashed lines*). We have also neglected the effects of finite ^{15}N T_1 values that interconvert amide ^{1}H multiplet components, leading to decreases in I^{CEST}. Such contributions are, however, small (Yuwen et al. 2017), especially considering the relatively short optimal T_{Ex} values for the L-optimized scheme.

Concluding remarks

Here we have presented L-optimized amide ^{1}H CEST experiments for studies of protonated protein systems in slow chemical exchange with a minor species. The experiments are based on recently published ^{1}H-CEST schemes that exploit the amide ^{15}N spin state to separate chemical and dipolar exchange processes (Yuwen et al. 2017) and take advantage of ideas developed for the BEST-family of experiments that selective excite only the amide protons of interest (Lescop et al. 2007). The utility of the approach is demonstrated with a number of applications to exchanging systems where it is shown that accurate ^{1}H excited state chemical shifts are readily obtained. As discussed previously, the presence of a large number of ^{1}H relaxation pathways, especially for protonated proteins, complicates the

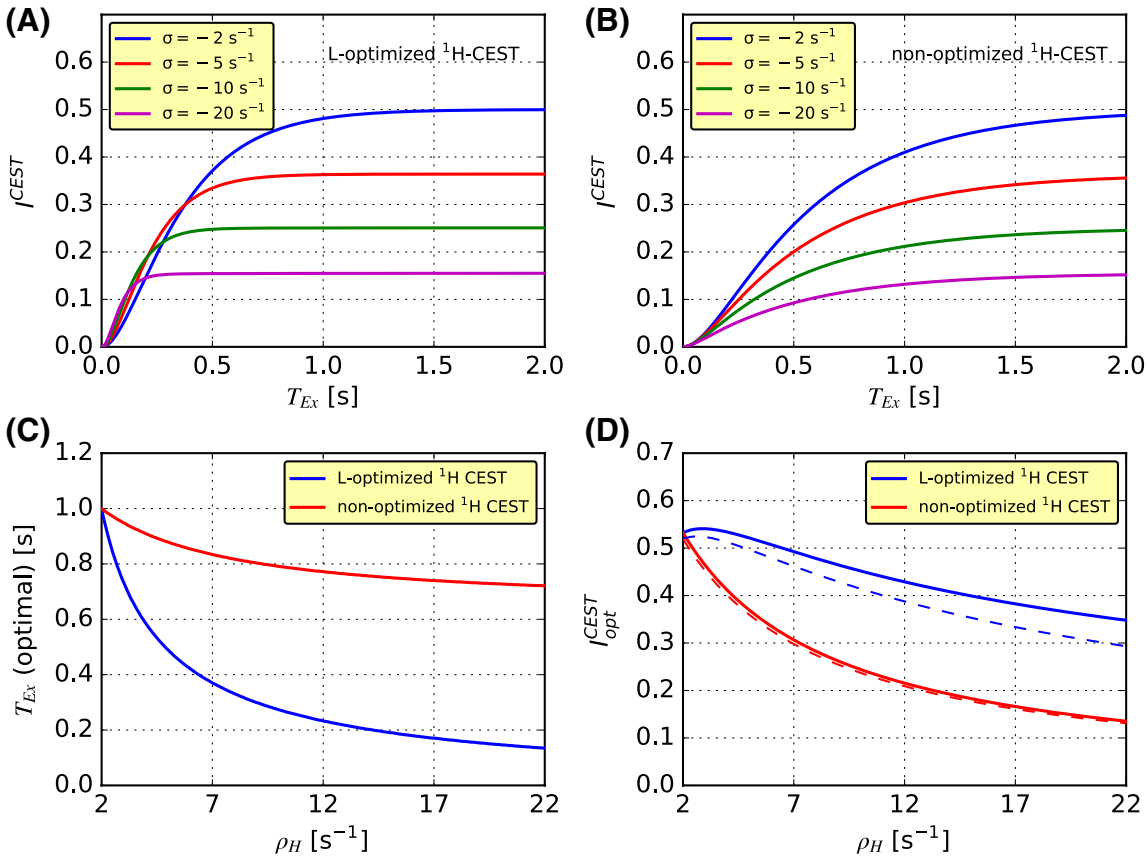

Fig. 8 **a, b** Build-up of I^{CEST} as a function of T_{Ex}, assuming scheme (i), $d_1 = 0$ s ($\kappa = 0$) using Eq. 2 and Eq S17 for the L-optimized and non-optimized ^{1}H-CEST, respectively. A value for $\rho_H = 2$ s^{-1} $- \sigma$ has been used. **c** Optimal values of T_{Ex} that generate the highest sensitivity per unit measurement time, evaluated from Eqs. 5 (L-optimized) and S18 (non-optimized), as a function of ρ_H. **d** I^{CEST}_{opt} *vs* ρ_H for L-optimized and non-optimized ^{1}H CEST (Yuwen et al. 2017) assuming that the duration of the pulse scheme is T_{Ex} ($\kappa = 0$), solid lines, or including an acquisition time $t_2 = 50$ ms and an additional duration of 50 ms that accounts for coherence transfer steps and ^{15}N labeling (t_1), *dashed lines*. In the simulations of the non-optimized experiment it is assumed that all ^{1}H longitudinal magnetization is 0 at the start of the t_2 acquisition period and that non-amide protons, that are in large excess over amide protons, relax back to their equilibrium value with a rate $\rho_S = 2$ s^{-1} (non-selective inversion). Exchange parameters $p_E = 2\%$, $k_{ex} = 200$ s^{-1} and been used and ^{15}N T_1 relaxation has been neglected

extraction of accurate (p_E, k_{ex}) values (Yuwen et al. 2017) that are best obtained from ^{15}N-CEST experiments (Vallurupalli et al. 2012). The L-optimized schemes presented here become particularly important for applications where it is not possible to perdeuterate the molecule of interest. While it is clear that perdeuteration is important for applications to large proteins, in studies of small protonated proteins where excellent quality spectra can be obtained, the L-optimized experiments may well generate CEST datasets with comparable or higher signal to noise ratios than the corresponding datasets obtained on highly deuterated molecules. These experiments will also be of utility in studies of exchange in RNA molecules using imino protons as probes, where the low density of protons relative to the case for proteins makes applications to protonated systems even more appealing in this class of biomolecule.

Acknowledgements This work was supported by grants from the Canadian Institutes of Health Research. L. E. K holds a Canada Research Chair in Biochemistry. Valuable discussions with Dr. Ashok Sekhar are acknowledged.

References

Anthis NJ, Clore GM (2015) Visualizing transient dark states by NMR spectroscopy. Q Rev Biophys 48:35–116. doi:10.1017/S0033583514000122

Banci L, Bertini I, Cramaro F, Del Conte R, Viezzoli MS (2002) The solution structure of reduced dimeric copper zinc superoxide dismutase. The structural effects of dimerization. Eur J Biochem 269:1905–1915. doi:10.1046/j.1432-1033.2002.02840.x

Bouvignies G, Kay LE (2012a) A 2D ^{13}C-CEST experiment for studying slowly exchanging protein systems using methyl probes: an application to protein folding. J Biomol NMR 53:303–310. doi:10.1007/s10858-012-9640-7

Bouvignies G, Kay LE (2012b) Measurement of proton chemical shifts in invisible states of slowly exchanging protein systems by chemical exchange saturation transfer. J Phys Chem B 116:14311–14317. doi:10.1021/jp311109u

Bouvignies G, Vallurupalli P, Kay LE (2014) Visualizing side chains of invisible protein conformers by solution NMR. J Mol Biol 426:763–774. doi:10.1016/j.jmb.2013.10.041

Carr HY, Purcell EM (1954) Effects of diffusion on free precession in nuclear magnetic resonance experiments. Phys Rev 94:630–638. doi:10.1103/PhysRev.94.630

Delaglio F, Grzesiek S, Vuister GW, Zhu G, Pfeifer J, Bax A (1995) NMRPipe: a multidimensional spectral processing system based on Unix pipes. J Biomol NMR 6:277–293. doi:10.1007/Bf00197809

Deverell C, Morgan RE, Strange JH (1970) Studies of chemical exchange by nuclear magnetic relaxation in rotating frame. Mol Phys 18:553–559. doi:10.1080/00268977000100611

Farrow NA, Zhang OW, Formankay JD, Kay LE (1994) A heteronuclear correlation experiment for simultaneous determination of ^{15}N longitudinal decay and chemical-exchange rates of systems in slow equilibrium. J Biomol NMR 4:727–734. doi:10.1007/Bf00404280

Favier A, Brutscher B (2011) Recovering lost magnetization: polarization enhancement in biomolecular NMR. J Biomol NMR 49:9–15. doi:10.1007/s10858-010-9461-5

Fawzi NL, Ying JF, Ghirlando R, Torchia DA, Clore GM (2011) Atomic-resolution dynamics on the surface of amyloid-beta protofibrils probed by solution NMR. Nature 480: 161–268. doi:10.1038/nature10577

Felli IC, Pierattelli R (2015) Spin-state-selective methods in solution- and solid-state biomolecular ^{13}C NMR. Prog Nucl Mag Res Sp 84:1–13. doi:10.1016/j.pnmrs.2014.10.001

Forsen S, Hoffman RA (1963) Study of moderately rapid chemical exchange reactions by means of nuclear magnetic double resonance. J Chem Phys 39:2892–2901. doi:10.1063/1.1734121

Freeman R, Hill HDW (1971) Fourier transform study of NMR spin-lattice relaxation by progressive-saturation. J Chem Phys 54:3367–3377. doi:10.1063/1.1675352

Geen H, Freeman R (1991) Band-selective radiofrequency pulses. J Magn Reson 93:93–141. doi:10.1016/0022-2364(91)90034-Q

Guenneugues M, Berthault P, Desvaux H (1999) A method for determining B_1 field inhomogeneity. Are the biases assumed in heteronuclear relaxation experiments usually underestimated? J Magn Reson 136:118–126. doi:10.1006/jmre.1998.1590

Gupta RK, Redfield AG (1970) Double nuclear magnetic resonance observation of electron exchange between ferricytochrome-C and ferrocytochrome-C. Science 169:1204–1206. doi:10.1126/science.169.3951.1204

Henzler-Wildman K, Kern D (2007) Dynamic personalities of proteins. Nature 450:964–972. doi:10.1038/nature06522

Karplus M, Kuriyan J (2005) Molecular dynamics and protein function. Proc Natl Acad Sci USA 102:6679–6685. doi:10.1073/pnas.0408930102

Kay LE, Keifer P, Saarinen T (1992) Pure absorption gradient enhanced heteronuclear single quantum correlation spectroscopy with improved sensitivity. J Am Chem Soc 114:10663–10665. doi:10.1021/ja00052a088

Kimsey IJ, Petzold K, Sathyamoorthy B, Stein ZW, Al-Hashimi HM (2015) Visualizing transient Watson-Crick-like mispairs in DNA and RNA duplexes. Nature 519:315–320. doi:10.1038/nature14227

Kupce E, Freeman R (1993) Polychromatic selective pulses. J Magn Reson Ser A 102:122–126. doi:10.1006/jmra.1993.1079

Lescop E, Schanda P, Brutscher B (2007) A set of BEST triple-resonance experiments for time-optimized protein resonance assignment. J Magn Reson 187:163–169. doi:10.1016/j.jmr.2007.04.002

Lescop E, Kern T, Brutscher B (2010) Guidelines for the use of band-selective radiofrequency pulses in hetero-nuclear NMR: example of longitudinal-relaxation-enhanced BEST-type ^{1}H–^{15}N correlation experiments. J Magn Reson 203:190–198. doi:10.1016/j.jmr.2009.12.001

Meiboom S, Gill D (1958) Modified spin-echo method for measuring nuclear relaxation times. Rev Sci Instrum 29:688–691. doi:10.1063/1.1716296

Mittermaier A, Kay LE (2006) New tools provide new insights in NMR studies of protein dynamics. Science 312:224–228. doi:10.1126/science.1124964

Montelione GT, Wagner G (1989) 2D chemical-exchange NMR-spectroscopy by proton-detected heteronuclear correlation. J Am Chem Soc 111:3096–3098. doi:10.1021/ja00190a072

Mulder FAA, Otten R, Scheek RM (2011) Origin and removal of mixed-phase artifacts in gradient sensitivity enhanced heteronuclear single quantum correlation spectra. J Biomol NMR 51:199–207. doi:10.1007/s10858-011-9554-9

Ottiger M, Delaglio F, Bax A (1998) Measurement of J and dipolar couplings from simplified two-dimensional NMR spectra. J Magn Reson 131:373–378. doi:10.1006/jmre.1998.1361

Palmer AG, Massi F (2006) Characterization of the dynamics of biomacromolecules using rotating-frame spin relaxation NMR spectroscopy. Chem Rev 106:1700–1719. doi:10.1021/cr0404287

Palmer AG, Kroenke CD, Loria JP (2001) Nuclear magnetic resonance methods for quantifying microsecond-to-millisecond motions in biological macromolecules. Method Enzymol 339:204–238. doi:10.1016/S0076-6879(01)39315-1

Pervushin K, Riek R, Wider G, Wuthrich K (1997) Attenuated T_2 relaxation by mutual cancellation of dipole-dipole coupling and chemical shift anisotropy indicates an avenue to NMR structures of very large biological macromolecules in solution. Proc Natl Acad Sci USA 94:12366–12371. doi:10.1073/pnas.94.23.12366

Pervushin KV, Wider G, Wuthrich K (1998) Single transition-to-single transition polarization transfer (ST2-PT) in [^{15}N, ^{1}H]-TROSY. J Biomol NMR 12:345–348. doi:10.1023/A:1008268930690

Pervushin K, Vogeli B, Eletsky A (2002) Longitudinal ^{1}H relaxation optimization in TROSY NMR spectroscopy. J Am Chem Soc 124:12898–12902. doi:10.1021/ja027149q

Schanda P, Van Melckebeke H, Brutscher B (2006) Speeding up three-dimensional protein NMR experiments to a few minutes. J Am Chem Soc 128:9042–9043. doi:10.1021/ja062025p

Schleucher J, Sattler M, Griesinger C (1993) Coherence selection by gradients without signal attenuation: Application to the 3-Dimensional HNCO experiment. Angew Chem Int Edit 32:1489–1491. doi:10.1002/anie.199314891

Sekhar A, Kay LE (2013) NMR paves the way for atomic level descriptions of sparsely populated, transiently formed biomolecular conformers. Proc Natl Acad Sci USA 110:12867–12874. doi:10.1073/pnas.1305688110

Sekhar A, Rosenzweig R, Bouvignies G, Kay LE (2015a) Mapping the conformation of a client protein through the Hsp70 functional cycle. Proc Natl Acad Sci USA 112:10395–10400. doi:10.1073/pnas.1508504112

Sekhar A, Rumfeldt JAO, Broom HR, Doyle CM, Bouvignies G, Meiering EM, Kay LE (2015b) Thermal fluctuations of immature SOD1 lead to separate folding and misfolding pathways. Elife 4:e07296. doi:10.7554/eLife.07296

Sekhar A, Rosenzweig R, Bouvignies G, Kay LE (2016) Hsp70 biases the folding pathways of client proteins. Proc Natl Acad Sci USA 113:E2794–E2801. doi:10.1073/pnas.1601846113

Sklenar V, Torchia D, Bax A (1987) Measurement of ^{13}C longitudinal relaxation using ^{1}H detection. J Magn Reson 73:375–379. doi:10.1016/0022-2364(87)90214-9

Smith MA, Hu H, Shaka AJ (2001) Improved broadband inversion performance for NMR in liquids. J Magn Reson 151:269–283. doi:10.1006/jmre.2001.2364

Tzeng SR, Kalodimos CG (2013) Allosteric inhibition through suppression of transient conformational states. Nat Chem Biol 9:462–465. doi:10.1038/Nchembio.1250

Vallurupalli P, Kay LE (2013) Probing slow chemical exchange at carbonyl sites in proteins by chemical exchange saturation transfer NMR spectroscopy. Angew Chem Int Edit 52:4156–4159. doi:10.1002/anie.201209118

Vallurupalli P, Bouvignies G, Kay LE (2012) Studying "invisible" excited protein states in slow exchange with a major state conformation. J Am Chem Soc 134:8148–8161. doi:10.1021/ja3001419

van Zijl PCM, Yadav NN (2011) Chemical exchange saturation transfer (CEST): What is in a name and what isn't? Magn Reson Med 65:927–948. doi:10.1002/mrm.22761

Ward KM, Aletras AH, Balaban RS (2000) A new class of contrast agents for MRI based on proton chemical exchange dependent saturation transfer (CEST). J Magn Reson 143:79–87. doi:10.1006/jmre.1999.1956

Wishart DS (2011) Interpreting protein chemical shift data. Prog Nucl Mag Res Sp 58:62–87. doi:10.1016/j.pnmrs.2010.07.004

Yang DW, Kay LE (1999) Improved ^{1}HN-detected triple resonance TROSY-based experiments. J Biomol NMR 13:3–10. doi:10.1023/A:1008329230975

Yang DW, Nagayama K (1996) A sensitivity-enhanced method for measuring heteronuclear long-range coupling constants from the displacement of signals in two 1D subspectra. J Magn Reson Ser A 118:117–121. doi:10.1006/jmra.1996.0017

Yuwen T, Sekhar A, Kay LE (2017) Separating dipolar and chemical exchange magnetization transfer processes in ^{1}H-CEST. Angew Chem Int Edit. doi:10.1002/anie.201610759

Zhao B, Zhang Q (2015) Measuring residual dipolar couplings in excited conformational states of nucleic acids by CEST NMR spectroscopy. J Am Chem Soc 137:13480–13483. doi:10.1021/jacs.5b09014

Zhao B, Hansen AL, Zhang Q (2014) Characterizing slow chemical exchange in nucleic acids by carbon CEST and low spin-lock field $R_{1\rho}$ NMR spectroscopy. J Am Chem Soc 136:20–23. doi:10.1021/ja409835y